

Article

Effect of the Shadow Pixels on Evapotranspiration Inversion of Vineyard: A High-Resolution UAV-Based and Ground-Based Remote Sensing Measurements

Saihong Lu ^{1,2,3} , Junjie Xuan ^{1,2,3}, Tong Zhang ^{1,2,3}, Xueer Bai ^{1,2,3}, Fei Tian ^{1,2,3,*} and Samuel Ortega-Farias ⁴ 

- ¹ Center for Agricultural Water Research in China, China Agricultural University, Beijing 100083, China; saihonglu@cau.edu.cn (S.L.); s20193091604@cau.edu.cn (J.X.); tongzhang@cau.edu.cn (T.Z.); bxe@cau.edu.cn (X.B.)
- ² Wuwei Experimental Station for Efficient Water Use in Agriculture, Ministry of Agriculture and Rural Affairs, Wuwei 733000, China
- ³ National Field Scientific Observation and Research Station on Efficient Water Use of Oasis Agriculture in Wuwei of Gansu Province, Wuwei 733000, China
- ⁴ Research Program on Adaptation of Agriculture to Climate Change (A2C2), Research and Extension Center for Irrigation and Agroclimatology (CITRA), Faculty of Agricultural Sciences, Universidad de Talca, Campus Talca, Talca 3460000, Chile; sortega@utalca.cl
- * Correspondence: feitian@cau.edu.cn; Tel.: +86-010-6273-6273

Abstract: Due to the proliferation of precision agriculture, the obstacle of estimating evapotranspiration (ET) and its components from shadow pixels acquired from remote sensing technology should not be neglected. To accurately detect shaded soil and leaf pixels and quantify the implications of shadow pixels on ET inversion, a two-year field-scale observation was carried out in the growing season for a pinot noir vineyard. Based on high-resolution remote sensing sensors covering visible light, thermal infrared, and multispectral light, the supervised classification was applied to detect shadow pixels. Then, we innovatively combined the normalized difference vegetation index with the three-temperature model to quantify the proportion of plant transpiration (T) and soil evaporation (E) in the vineyard ecosystem. Finally, evaluated with the eddy covariance system, we clarified the implications of the shadow pixels on the ET estimation and the spatiotemporal patterns of ET in a vineyard system by considering where shadow pixels were presented. Results indicated that the shadow detection process significantly improved reliable assessment of ET and its components. (1) The shaded soil pixels misled the land cover classification, with the mean canopy cover ignoring shadows 1.68–1.70 times more often than that of shaded area removal; the estimation accuracy of ET can be improved by 4.59–6.82% after considering the effect of shaded soil pixels; and the accuracy can be improved by 0.28–0.89% after multispectral correction. (2) There was a 2 °C canopy temperature discrepancy between sunlit leaves and shaded leaves, meaning that the estimation accuracy of T can be improved by 1.38–7.16% after considering the effect of shaded canopy pixels. (3) Simultaneously, the characteristics showed that there was heterogeneity of ET in the vineyard spatially and that E and T fluxes accounted for 238.05 and 208.79 W·m⁻², respectively; the diurnal variation represented a single-peak curve, with a mean of 0.26 mm/h. Our findings provide a better understanding of the influences of shadow pixels on ET estimation using remote sensing techniques.

Keywords: vineyard; evapotranspiration; shadow pixel; UAV; remote sensing



Citation: Lu, S.; Xuan, J.; Zhang, T.; Bai, X.; Tian, F.; Ortega-Farias, S. Effect of the Shadow Pixels on Evapotranspiration Inversion of Vineyard: A High-Resolution UAV-Based and Ground-Based Remote Sensing Measurements. *Remote Sens.* **2022**, *14*, 2259. <https://doi.org/10.3390/rs14092259>

Academic Editors: Zhongjing Wang, Lu Zhang and Lei Wang

Received: 6 April 2022

Accepted: 5 May 2022

Published: 7 May 2022

Publisher's Note: MDPI stays neutral with regard to jurisdictional claims in published maps and institutional affiliations.



Copyright: © 2022 by the authors. Licensee MDPI, Basel, Switzerland. This article is an open access article distributed under the terms and conditions of the Creative Commons Attribution (CC BY) license (<https://creativecommons.org/licenses/by/4.0/>).

1. Introduction

As one of the characteristic economic fruits in Northwest China, grape has high economic value [1,2]. However, grape yield has been negatively affected by drought and high evapotranspiration (ET) [3]. On the one hand, the spatial and temporal patterns of precipitation are uneven, with more rainfall concentrated in summer and less in spring, which has a serious impact on the quality of grape [4]. Thus, irrigation is used by growers

to alleviate environmental constraints. Evapotranspiration is composed of soil evaporation (E) and plant transpiration (T), which is an important component of energy and water balances in farmland ecosystem [5]. ET is the main method of agricultural water dissipation, especially in the arid inland river basin. Rosenberg et al. [6] reported that more than 90% of water resources return to the atmosphere through ET after precipitation reaches the ground, and it was further demonstrated that T accounted for about 57.2% of terrestrial ET [7], both of them indicating that it is critical to accurately estimate crop water consumption. In the soil–plant–atmosphere continuum, crops absorb irrigation water through their roots and lose water to the atmosphere through transpiration [8]; accurate quantification of T can provide a basis for making irrigation schemes and developing precision agriculture.

In recent years, measurement of grape transpiration has certainly garnered a lot of attention. Conventional methods such as crop coefficient method [9,10] and equilibrium Bowen ratio–energy method [11] have ineluctable flaws. Among them, the determination of grape transpiration using either the single-crop coefficient method or the double-crop coefficient method is affected by crop growth conditions, meteorological factors, and so forth, and the estimation effect of different growth stages fluctuates greatly [4] and has been reported to be underestimated by about 17% [12]. The equilibrium Bowen ratio–energy method is based on the exchange of water and heat on the underlying surface [11] and is widely applied due to few parameters needing to be measured, but its accuracy is greatly affected by the underlying surface, soil conditions, and the use of instruments [13]. More importantly, neither method can accurately estimate the actual water consumption within the regional scope. As discussed above, it can be seen that traditional methods no longer meet the precision requirement of regional crop transpiration rate estimation in the farmland microclimate environment [14]. Currently, there are few studies on the water consumption of vineyard transpiration at the spatial scale because most existing studies focus on the temporal scale [4,11,12], precisely reflecting that estimating the spatial heterogeneity of vineyard evapotranspiration is still a source of concern.

As for the limitation of using “point” observation instead of “region” observation in the traditional estimation method of evapotranspiration, Brown et al. [15] used thermal infrared (TIR) remote sensing (RS) to establish a crop impedance–evapotranspiration model based on the principle of crop impedance and energy balance, which overcame this shortcoming and became the theoretical basis for the application of thermal infrared remote sensing to an evapotranspiration model [16]. RS has the superiorities of accuracy, wide observation range, and visualization, especially with the development of handheld imagery [17] and unmanned aerial vehicle (UAV) imagery [18,19]. Remote sensors such as regular RGB (red, green, blue), thermal infrared, and multispectral imaging cameras were placed on a UAV to collect high-resolution data of the Earth’s surface in a field-scale trial, making it possible for regional crop transpiration data to be successfully retrieved by combining this technique with a model. Among them, the most prominent approach is the two-layer model, which can divide vegetation and soil into two independent parts [20]. For example, the three-temperature model (3T model) has been proposed to estimate ET and its components by Qiu et al. [14,21,22]. This model contains fewer parameters, and these parameters are easy to obtain with RS or a meteorological station; additionally, the concepts of imitation dry soil and imitation canopy have been introduced to avoid difficulties with data acquisition such as aerodynamic impedance [22], implying the wide feasibility and applicability in E and T quantifications [23–26].

In calculations using the two-layer model, E and T are calculated, respectively, so the coupling law between transpiration and evaporation can be better described. However, suffering from issues with the shaded soil or canopy, the actual situation of ET inversion based on TIR is more complicated and greatly hinders the feedback of thermal information [27–29]. Multiple studies have made a lot of contributions to remove these shaded pixels. For example, based on UAV RS, Bellvert et al. [30] and Ortega-Farias et al. [20] considered how mixed pixels and shaded soil pixels may affect the information in an image, and only pure canopy vegetation pixels were selected, but the mechanism of shaded soil

from the TIR information remained unclear. On the other side, the inner shaded canopy pixels cannot be detected when the TIR imagery is captured on the canopy, resulting in mixed pixels. In this regard, Miura et al. [31] and Heiskanen et al. [32] defined a specific wavelength range as the shadow but could not separate shaded canopy from shaded soil; Tomas et al. [29] proposed a methodology for the automatic coregistration of thermal and multispectral images to remove shadow canopy pixels, but the crop transpiration difference between the shaded canopy and sunlit canopy was difficult to distinguish on an aviation scale. Meanwhile, the performance of four different shadow detection methods in UAV imagery has been detected, and results concluded that the supervised classification method had the best performance [33]. Hence, to identify the influence of shaded soil and shaded canopy pixels on vineyard ET estimation, a combined technique using ground-based and UAV-based thermal infrared was applied in this study.

The objectives in this study are to (1) evaluate the influences of shaded soil on the quantification of vineyard E and T based on UAV remote sensing, (2) investigate the differences of T in shaded canopy and sunlit canopy based on ground TIR imagery, and finally (3) quantify the spatiotemporal characteristics of vineyard transpiration using UAV-based and ground-based TIR remote sensing combined with the 3T mode.

2. Materials and Methods

2.1. Experimental Design

The study was carried out during the 2019 and 2020 growing seasons in a vineyard at the Mogao winery ($37^{\circ}49' N$, $102^{\circ}52' E$, elevation 1588 m) located in Liangzhou District, Wuwei City, Gansu Province, Northwest China (Figure 1). This region typically has a temperate and arid climate. With rare rainfall but intensive evaporation, the average annual precipitation and the average annual surface evaporation are approximately 182 mm and 2200 mm, respectively. The mean annual temperature is around $8^{\circ}C$; the solar-thermal resources in this area are abundant, with more than 3000 h of annual sunshine duration; and the annual frost-free period is more than 150 days [34]. The natural condition of this station is optimum for the growth of grapes.

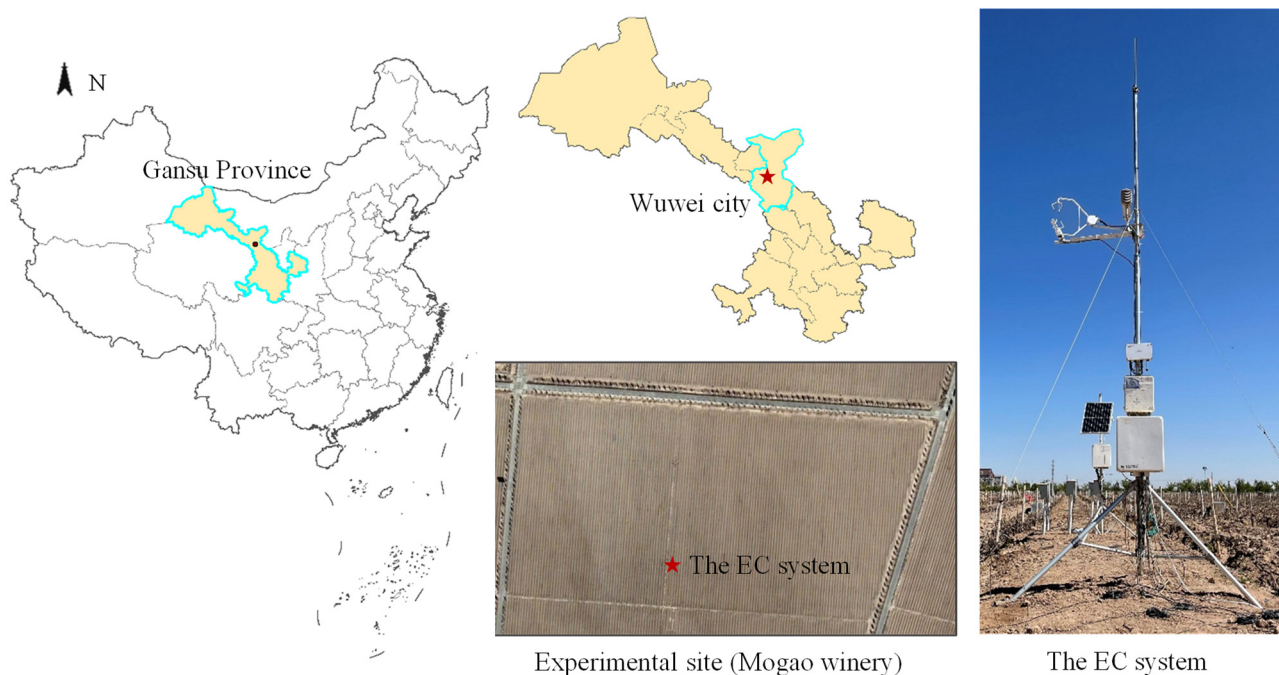


Figure 1. Location of the experimental site.

The experimental plot measuring 12.6 ha in area was a pinot noir (*Vitis vinifera* L.) commercial vineyard, which was planted from 2014. The distances of row spacing and

plant spacing were 3.3 m and 0.5 m, respectively, and the vineyard was a sparse vegetation ecosystem, with no vegetation cover between the vines except for bare soil. The vineyard used drip irrigation, which was carried out by a pipe suspended 0.4 m above the ground. Each pipe was covered with emitters, and the distance between the emitters was 0.4 m; meanwhile, the flow rate of the emitters was 3 L/h. The grape growth season was from the bud in late April until the decline of the leaf in late September, and the grapes were usually harvested in mid-September. Field work such as pruning, weeding, and ploughing was carried out in time to ensure the growth of the grapes.

2.2. Data Acquisition and Processing

2.2.1. Remote Sensing Data Acquisition

The remote sensing observations yielded visible and thermal images of grape, which were obtained from the aeronautic and ground scale in this study (Figure 2). The measurements were conducted on 6 June, 6 July, 12 July, 16 July, 22 July 2019, and 26 June, 7 July, 8 July, 28 July, 13 August, and 18 August 2020, and UAV-based observations only were collected at 13:00 h. The experiment days were cloudless, and the wind speed was lower than $8 \text{ m}\cdot\text{s}^{-1}$, which were suitable conditions for data collection. Each capture had more than two replicates for both the UAV-based and ground-based observations, and the best-quality images were singled out for further analysis.

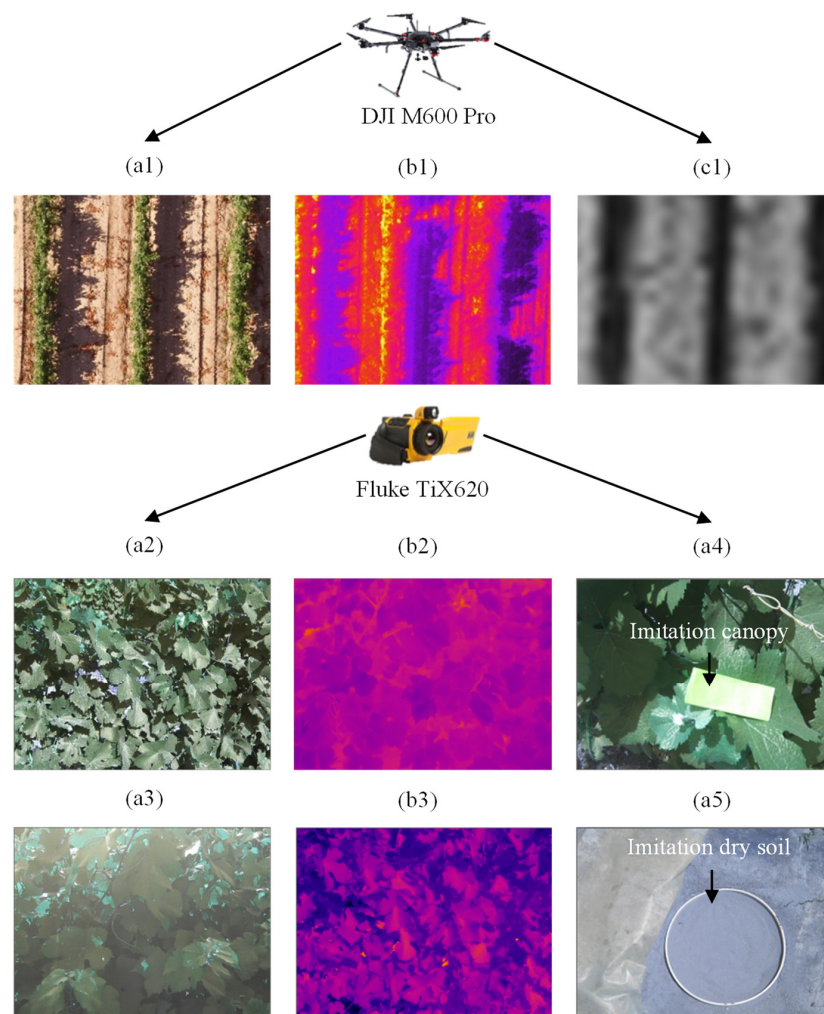


Figure 2. The observation of experimental plot based on UAV and ground remote sensing: (a1)–(a5) the visible-light, (b1)–(b3) thermal infrared, and (c1) multispectral images of vineyard. Specially, (a4,a5) are the RGB images of imitation canopy and imitation dry soil (see Section 2.3.1).

For the UAV-based observation, a six-axis aerial vehicle platform (DJI Matrice 600 Pro) loaded with a cloud-borne camera (DJI Zenmuse Z3), TIR camera (FLIR Vue Pro 640) and multispectral camera (MicaSense RedEdge-MX) was used to collect the RGB, thermal infrared, and multispectral images of the vineyard (Figure 2(a1,b1,c1)). The digital camera had a high level accuracy of $\pm 0.03^\circ$; the thermal infrared camera had a measurement wavelength range from 7.5 to 13.5 μm , with a sensitivity and lens focal length of 0.05 $^\circ\text{C}$ and 19 mm, respectively. The multispectral camera contained five spectral bands (blue, green, red, red edge, and near-infrared) and took pictures once per second. Meanwhile, the spatial resolution of the visible-light, TIR, and multispectral cameras was 640×512 pixels, 12 million pixels, and 8 cm/pixel at 120 m, respectively. In order to prevent the sensors from being damaged by the sun during flight, the cameras were set to shoot vertically from the ground. The classification of vegetation, bare soil, and shaded soil in the images was distinct, as presented in Figure 2(a1). The UAV had a horizontal and vertical hovering accuracy of ± 1.5 m and ± 0.5 m, respectively.

For the ground-based observation, a handheld TIR imager was used to capture both high-resolution thermal infrared and RGB images at 1.5–2 m above the grape canopies (Fluke IR Flex Cam TiX620, Fluke Corp., Everett, WA, USA). The imager had two cameras to collect images: a visible-light camera and a high-resolution TIR camera, as demonstrated in Figure 2. The visible-light digital camera had a spatial resolution of 8 megapixels and up to 32 times digital zoom; the TIR image sensor had a spatial resolution of 640×480 pixels and had an accuracy, sensitivity, and measuring wavelength of ± 2 $^\circ\text{C}$, 0.05 $^\circ\text{C}$, and 7.5–14 μm , respectively. Finally, the emissivity and background temperature for the grape canopies were set to 0.95 and 22.0 $^\circ\text{C}$, respectively [17,35].

2.2.2. Meteorological Data Acquisition

A four-component net radiometer (Kipp & Zonen CNR4, Delft, The Netherlands) and the Bowen ratio system were used to collect the radiation data (i.e., net longwave and net shortwave radiation) with a data recording frequency of 5 min, and then the measurements were used to calculate the net surface radiation flux (R_n , Equation (7)). Meanwhile, a standard automatic weather station (HOBO H21001, Onset Computer Corp., Cape Cod, MA, USA) continuously measured meteorological data, such as air temperature (T_a) and precipitation (P), and the data recording frequency was 15 min.

During the experiment, the total precipitation of every growing season recorded was about 131.6 mm, indicating that the growth of grapes depended on irrigation. The R_n and T_a increased in the morning and then decreased after midday (Figure 3). Moreover, it can be seen that the R_n reached its maximum value at noon, but there was an obvious lag in the air temperature, the T_a , which reached its peak after a certain accumulation of energy. Both of them jointly affected the transpiration rate of vegetation.

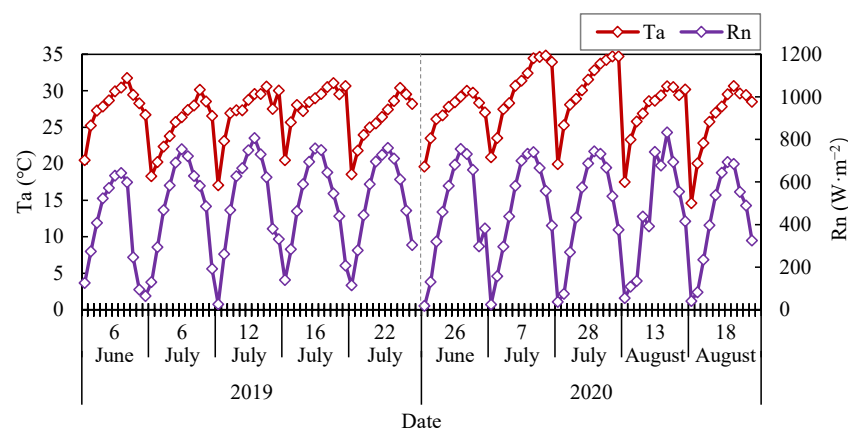


Figure 3. The diurnal variations of air temperature (T_a) and net radiation (R_n) in the investigation days.

2.2.3. Eddy Covariance

The eddy covariance (EC) open-flux system was set up in the vineyard, and its position is indicated in Figure 1. An EC tower was installed at the center of the grape ridges, and the height of the grape canopy was about 1.13–1.42 m from the ground. Therefore, in order to fully measure the water–carbon flux above and below the canopy, the erection height of the EC tower was 4 m, and the sampling frequency and the interval of data recording were 10 Hz and 30 min, respectively. The system included an open-circuit CO₂/H₂O infrared gas analyzer (LI-COR Inc., Lincoln, NE, USA) with high-speed, high-precision, and non-dispersive features that can accurately measure the density of carbon dioxide and water vapor in turbulent air for subsequent validation. The observation data were collected by a CR5000 data collector (Campbell Company, Camden, NJ, USA) with the same frequency and timescale.

2.3. Methods

2.3.1. ET Remote Sensing Estimation Method

3T Model

The transpiration rate of grape was estimated using the 3T model, which is a two-source evapotranspiration method for estimating evapotranspiration and its components of soil evaporation and vegetation transpiration based on the idea of land–surface energy balance [14,21,36,37]. The key parameters required by this method include land surface temperature, imitation surface temperature, air temperature, net radiation, and soil heat flux. The aerodynamic impedance, which is difficult to retrieve using remote sensing, was eliminated, meaning that the application was convenient and the stability was high. This approach has been extensively applied in arid and semiarid areas with a modeled absolute error and a relative error of 0.08 mm/d and 10.67%, respectively, in the Heihe River Basin area [35], compared with flux tower ET.

Since this is a mature model and the theory has been described in detail by previous studies [14,24], only a brief description of the plant transpiration and soil evaporation calculation models to calculate T and E, respectively, are presented here.

When vegetation covers the land, the equation to calculate the T in the 3T model can be expressed as follows:

$$LT = R_{n,c} - H_c \quad (1)$$

where the LT is the latent heat flux consumed by the transpiration of grape ($W \cdot m^{-2}$) and L is the vaporization latent heat with a constant of $2.45 \times 10^6 W \cdot m^{-2} \cdot mm^{-1}$. Furthermore, H_c is the grape sensible heat flux and can be computed as seen in Equation (2) [35]:

$$H_c = \frac{\rho \times C_p \times (T_c - T_a)}{r_a} \quad (2)$$

$$r_a = \frac{\rho \times C_p \times (T_{ci} - T_a)}{R_{n,ci}} \quad (3)$$

where the ρ and C_p are the air density ($kg \cdot m^{-3}$) and the specific heat at constant pressure ($MJ \cdot kg^{-1} \cdot ^\circ C^{-1}$), respectively. The r_a is the aerodynamic resistance (sm^{-1}), namely, the air layer's diffusion resistance, and the T_{ci} is the imitation canopy temperature, which describes the canopy without transpiration. Moreover, for the UAV-based calculation, we considered using the maximum canopy temperature to replace the imitation canopy temperature due to the difficulty of capturing the imitation canopy [38]. The subscripts "a", "c", and "ci" indicate the air, canopy, and imitation canopy, respectively. The imitation canopy and soil experimental arrangement are shown in Figure 2(a4,a5) as an example. Imitation leaf was made of green dry green paper and placed horizontally on the grape canopy; the imitation soil was sifted into fine-grained soil from local soil, and naturally dried for three days before being loaded into plastic cylinders and buried.

By combining Equations (1)–(3), the T can be estimated using the following equation:

$$LT = R_n - R_{n,ci} \frac{T_c - T_a}{T_{ci} - T_a} \quad (4)$$

Meanwhile, based on the principle of energy balance, when bare soil covers the land, soil evaporation submodules can be represented as

$$LE = R_{n,s} - G_s - (R_{n,si} - G_{si}) \frac{T_s - T_a}{T_{si} - T_a} \quad (5)$$

where $R_{n,s}$ and $R_{n,si}$ are the net soil radiation and imitation dry soil radiation, respectively; G_s and G_{si} are the soil heat flux and imitation soil heat flux, respectively.

Moreover, the canopy coverage (f) is introduced and the latent heat flux (LET) is obtained by combining the two submodules (Equations (4) and (5)):

$$LET = (1 - f)LE + f \times LT \quad (6)$$

Radiation Flux and Heat Flux Calculations

As described above, one of the key parameters of the 3T model was calculated by the following equation:

$$R_n = R_{ld} + R_{sd} - R_{lu} - R_{su} \quad (7)$$

where R_n is the net solar radiation; R_{ld} and R_{sd} are the downward longwave and short-wave radiations, respectively; and R_{lu} and R_{su} are the upward longwave and shortwave radiations, respectively, all with the unit $W \cdot m^{-2}$. Since the scale of this experiment was meters, we approximately equated the net imitation canopy radiation ($R_{n,i}$) and the net canopy radiation ($R_{n,c}$) with the R_n [21].

In addition, the net soil radiation and imitation soil radiation can be described as follows:

$$R_{n,s}(R_{n,si}) = R_{ld} - R_{lu} + (1 - \alpha)R_{sd} \quad (8)$$

where α is the albedo of the drying soil surface. In previous studies [14,39], when $\alpha = 0.25$, we calculate the $R_{n,s}$; when $\alpha = 0.275$, we calculate the $R_{n,si}$, and units are in $W \cdot m^{-2}$.

Usually the soil heat flux and imitation soil heat flux ($W \cdot m^{-2}$) can be estimated using the empirical formula, and according to Qiu et al. [14], G_s and G_{si} can be calculated as follows: $G_s = 0.2R_{n,s}$; $G_{si} = 0.1R_{n,si}$.

2.3.2. Pure Canopy Pixel Extraction

Canopy coverage (f) is the ratio of the vertical projection of vegetation onto the land surface to the total area of crops; the higher the canopy coverage, the stronger the ability of crops to intercept light. Furthermore, it can also be used as an indicator of crop growth, and it plays an important role in quantifying ET in this study.

High-resolution images taken by UAVs with thermal infrared sensors are used to extract the region of interest based on visual interpretation and supervised classification to obtain vegetation, soil, and other partitions. The f is as follows:

$$f = \frac{\text{Number}_{\text{plant pixels}}}{\text{Number}_{\text{total pixels}}} \quad (9)$$

In addition, existing studies have shown that canopy coverage can be accurately extracted by using the vegetation index extracted by multispectral or hyperspectral sensors carried on the UAV and different classification methods according to different object vegetation index thresholds. The normalized difference vegetation index (NDVI) is the

most widely recognized vegetation index for extracting pure vegetation pixels [40,41]; thus, the f can be represented as follows [42]:

$$\text{NDVI} = \frac{\text{NIR} - \text{R}}{\text{NIR} + \text{R}} \quad (10)$$

$$f = \frac{\text{NDVI} - \text{NDVI}_{\text{soil}}}{\text{NDVI}_{\text{veg}} - \text{NDVI}_{\text{soil}}} \quad (11)$$

where NIR and R are the values of near infrared and red channels, respectively; NDVI_{veg} and $\text{NDVI}_{\text{soil}}$ are the NDVI values of the pixel completely covered by vegetation and bare soil, respectively.

Therefore, in order to obtain pure vegetation and soil pixels, there are four results from the division. We first used the minimum distance method of supervised classification to process the thermal infrared images captured by the UAV and then visually interpreted the images combined with the visible-light images: (1) divided into the two classes of vegetation and soil; (2) divided into three classes of vegetation, bare soil (not included in the scope of the calculation), and shaded soil. The canopy coverage estimated by the NDVI is considered to estimate ET, so there are two other types of regions of interest: (3) only vegetation and bare soil; (4) vegetation, shaded soil, and bare soil.

2.3.3. Statistical Analysis

Three evaluation indexes, namely, coefficient of determination (R^2), root-mean-square error (RMSE), and relative root-mean-square error (rRMSE), were used to assess the quality of the model in this study.

2.3.4. Processing and Mapping of the Data

The thermal infrared images collected by the UAV were input into the FLIR Tools image processing software and were processed applying geometric and radiometric corrections. We used PhotoScan and Pix4D software to splice the TIR, RGB, and multispectral data to make them reflect the information of the entire study area, and the characteristic temperature of the TIR data was selected using FLIR Tools, with its temperature matrix file derived simultaneously. Then, we used the minimum distance method under the supervised classification category of ENVI 4.8 software (image analysis software, Exelis Visual Information Solutions, Boulder, CO, USA) to accurately identify ground objects. In this stage, the most important step was dividing the region of interest into two or three classes. Otherwise, the NDVI was generated using the raster calculator from the extracted multispectral information for canopy cover estimation. In the end, the hydrothermal flux and its components were calculated based on the three-temperature model.

Compared with the UAV-based data, the processing of the ground-based data was simpler. Without correction and splicing, the remote sensing images were analyzed using SmartView 4.3, a thermal infrared image processing software, and then the land surface temperature and visible-light data of the vineyard was extracted. After that, we outlined the region of interest (the grape canopies) for each image using ENVI 4.8. Furthermore, the above parameters combined with the meteorological data were substituted into the 3T model to quantitatively estimate the transpiration rate. The details of this workflow are shown in Figure 4.

3. Results

3.1. Variability of Vineyard Thermal Imagery

Figure 5 presents the thermal image of the vineyard collected at 13:00 h on 6 June 2019 and acquired by a UAV. There was marked significant spatial heterogeneity in land surface temperatures throughout the vineyard, especially in the discrepancies between soil and vegetation. The maximum LST corresponded with the bare soil pixels, reaching values of over 50 °C. The temperature of the grapevine canopies ranged from 24 °C to 40.4 °C,

which was greater than the air temperature by a maximum difference of 10 °C (i.e., the T_a with a value of 29.9 °C as shown in Figure 3). On the other hand, it is notable that the surface temperature of different areas in the experimental area was also quite variable. For example, the average temperature of plot 1 was 3.1 °C higher than that of plot 2.

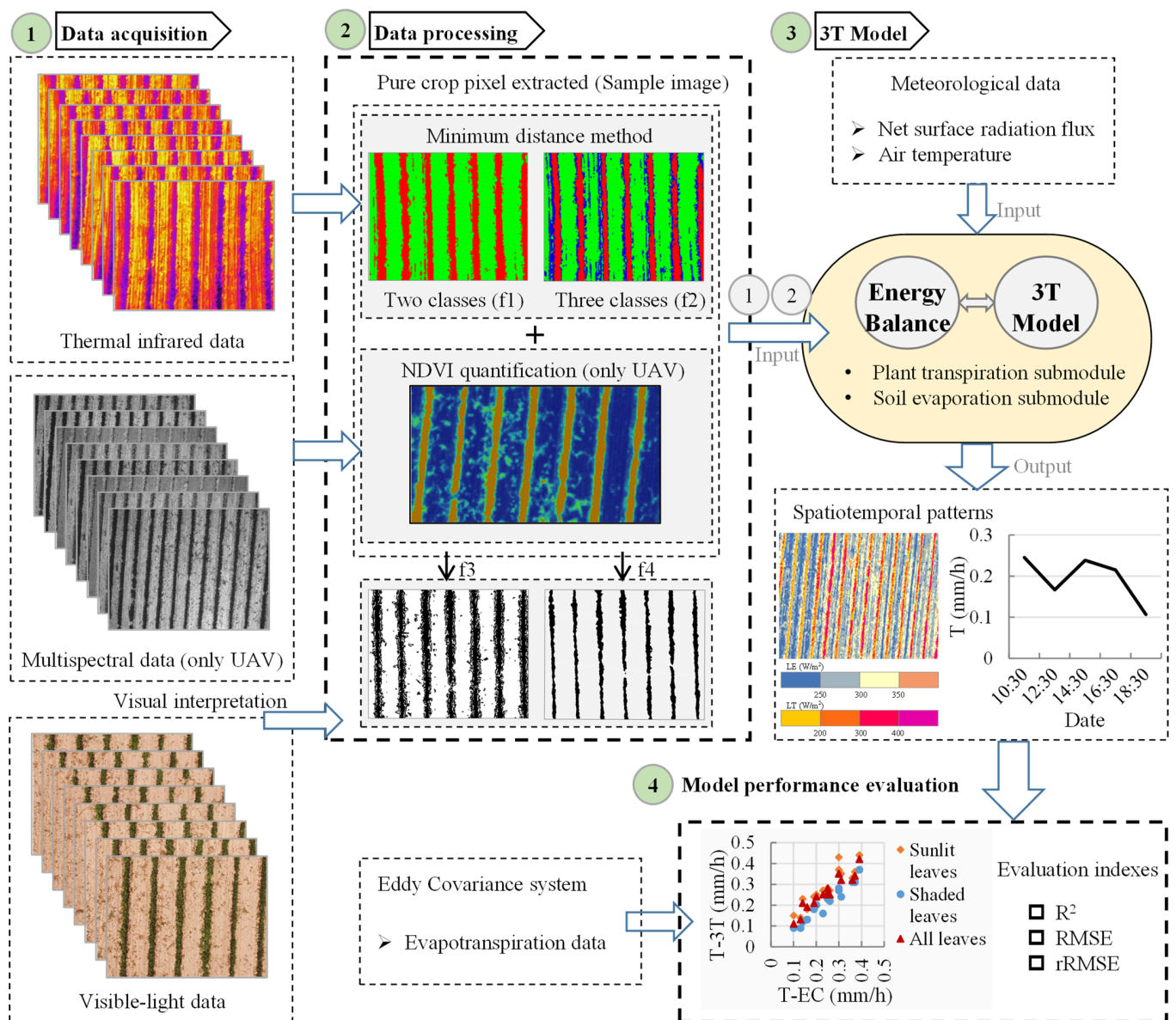


Figure 4. The schematic diagram of data processing for ET estimation.

3.2. Effect of the Shaded Soil Pixels on Vineyard Evapotranspiration

3.2.1. Thermal Characteristic of Shaded Soil Pixels

The visible-light and thermal infrared images obtained at different UAV flying altitudes in the sparse vineyard and the corresponding frequency distribution are shown in Figure 6. After magnifying the RGB image of a row of grapevines, we found that most of the vegetation pixels and bare soil pixels were absolutely clear, but it was necessary to consider the division of shaded soil pixels, which is also an important factor influencing the accurate acquisition of evapotranspiration in the study area. The recognition of shaded soil pixels decreased with the increase of flight height. It could be distinctly identified at 40 m and 80 m flying altitude, but it was relatively blurred at 120 m.

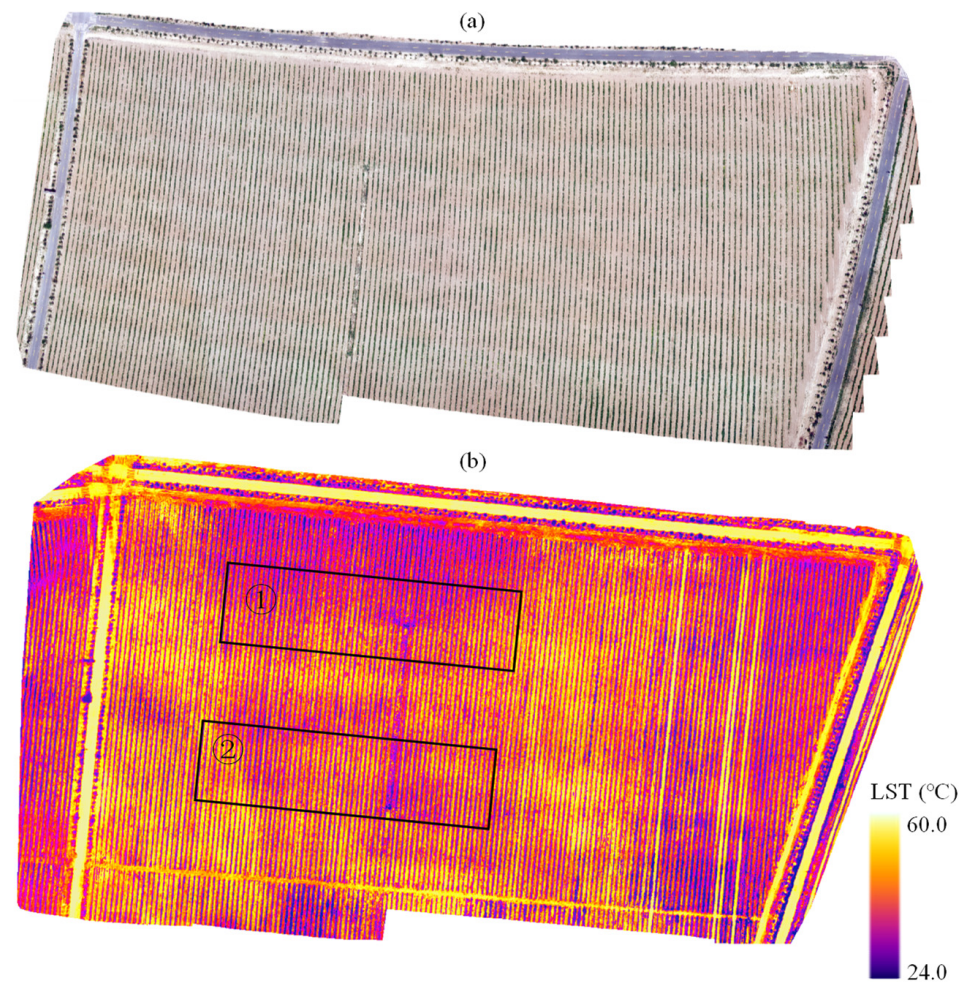


Figure 5. Airborne (a) visible-light and (b) thermal image obtained over the study vineyard at 13:00 on 6 June 2019. The black rectangle marked were set up for statistics.

Meanwhile, we found from the thermal infrared images that the information between pure soil and vegetation pixels differed greatly (Figure 6b), which has also been indicated in Figure 5. The vegetation pixels were deep purple while the soil pixels were bright yellow, and the values of LST were concentrated in the ranges of 26–38 °C and 42–50 °C, respectively. Specifically, two peaks in the frequency distribution diagram are presented in Figure 6c. More importantly, the soil surface temperature was significantly higher than the canopy surface temperature at observation heights of 2 m, 40 m, 80 m, and 120 m, and the LST of bare soil was 7.2 °C, 12.9 °C, 3.9 °C, and 14 °C higher than that of vegetation. From the perspective of the UAV, the area of bare soil was larger than the area of grape compared to the ground-based data, so the peaks representing soil pixels appear taller and wider in the histograms. In addition, illustrating the different contributions of canopy and background soil temperatures to the overall temperature histogram, it can be seen that due to the influence of the mixed pixels and the shaded soil pixels, the two peaks are moving closer to each other and cannot be separated as in the ground-based RS image (Figure 6(c4)). Obviously, the temperature characteristics of these pixels were between the pure vegetation and soil pixels, and the number of pixels increased with the increase of observation height, which in the form of the frequency increased from 0.07% (40 m) to 0.18% (120 m).

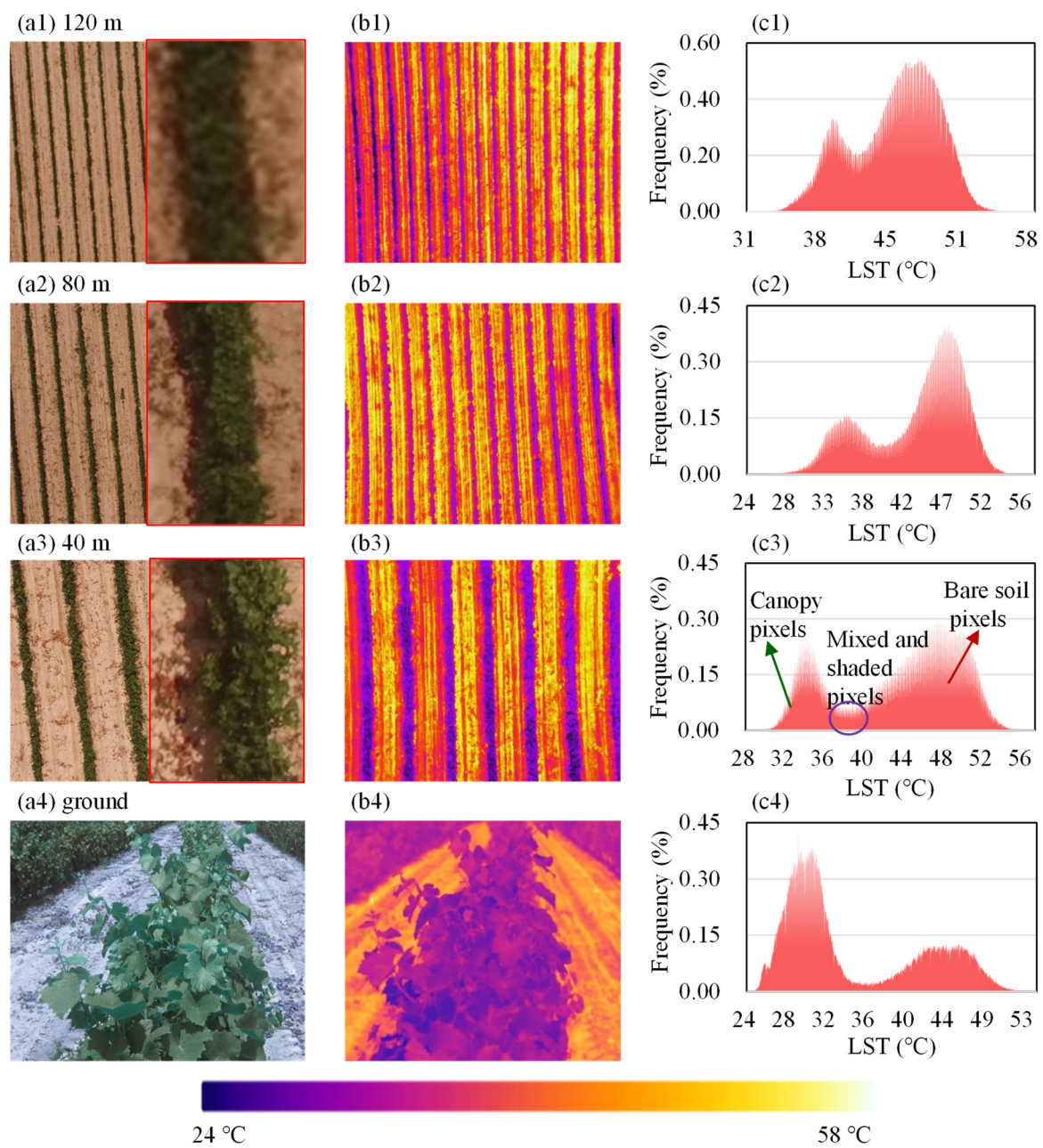


Figure 6. Map of the (a) visible light, (b) land surface temperature (LST), and (c) their frequency histograms of vineyard at different observation heights: (1) 120 m; (2) 80 m; (3) 40 m; and (4) 2 m. The data of 120 m were taken at 13:00 on 12 July 2019; 80 m and 40 m were the samples acquired at 13:00 and 13:30 on 16 July 2019, respectively; the ground data were acquired at 13:14 on 16 July 2019.

According to the above results, it is implied that if a shaded soil pixel is divided into a vegetation pixel, the canopy temperature will rise, thus affecting the transpiration rate estimated by the 3T model. Similarly, the estimation accuracy would eventually be affected if it were divided into bare soil pixels. Thus, removing the influence of shaded soil pixels becomes distinct and critical.

3.2.2. Extraction of Pure Pixels

Taking one image acquired by the UAV at a flight altitude of 40 m as an example, the results obtained using the four classification methods are shown in Figure 7. It can be seen that there were great differences between the two results obtained by the supervised

classification method (Figure 7a,b); among them, the shadow pixels affect the canopy coverage. Under classification method 1, the number of vegetation and soil pixels amounted to 105,499 and 222,181, respectively. Under classification method 2, the number of vegetation, soil, and shaded pixels were 73,218, 196,643, and 57,819, respectively. Obviously, when only two categories were divided, the shaded and mixed pixels were divided into vegetation or bare soil. After the three categories, the vegetation pixels decreased by 30.6%, and the soil pixels had the same situation, with 7.8% of the shadow and mixed pixels being divided into soil pixels. Furthermore, the NDVI measurements of shaded and mixed pixels were between 0.22 and 0.50, while the NDVI measurements of the pure grape canopy pixels were greater than 0.5, with an average of 0.79.

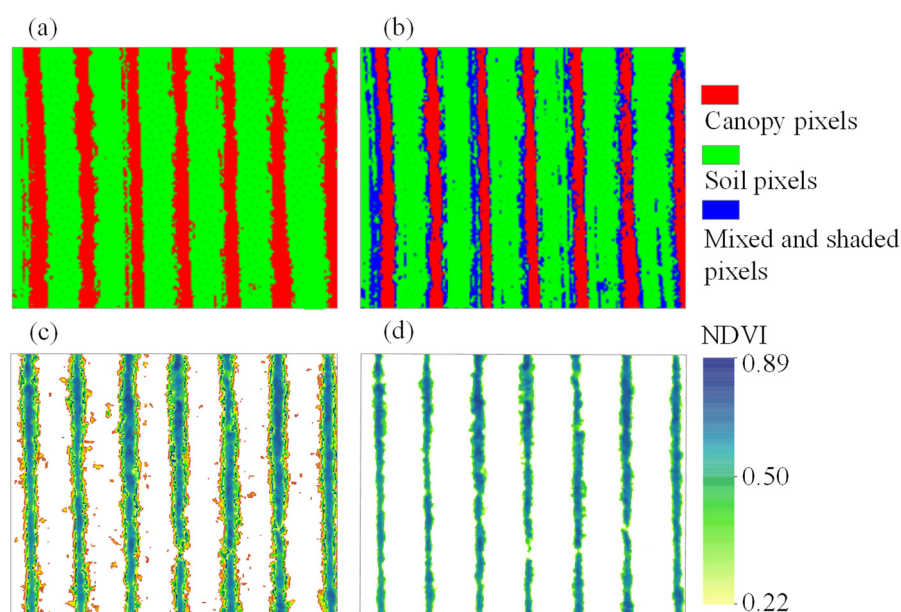


Figure 7. Example of spatial variability of four types of pixel classifications: (a,b) are the distributions of not considering and considering the shaded soil based on supervised classification, respectively; (c,d) are the distributions of not considering and considering the shaded soil based on the supervised classification and normalized difference vegetation index (NDVI), respectively.

Figure 8 quantifies four types of canopy cover in the vineyard, corresponding to the four classifications described above. During all fieldwork, f showed a trend of first increasing and then decreasing. Meanwhile, it is worth noting that with the increase of flight height, the f_1 of supervised classification results increases. To be more specific, the values of f_1 were 23.90%, 25.39%, and 26.54% at 40 m, 80 m, and 120 m observation height, respectively. While taking mixed and shaded pixels into consideration, the pattern of canopy cover was the opposite, with corresponding values of 16.28%, 15.82%, and 12.57%, which means that the number of mixed pixels was more with the lower spatial resolution, and they were always easily classified as vegetation pixels. Otherwise, compared with consideration of the shadow pixels, the f calculated by two classes was larger, and the mean- f_1 and mean- f_3 were 1.70 and 1.68 times the mean- f_2 and mean- f_4 , respectively. Compared with consideration of multispectral correction, the f calculated by supervised classification was larger, and the mean- f_1 and mean- f_2 were 1.24 and 1.23 times the mean- f_3 and mean- f_4 , respectively. Meanwhile, the gap between them was larger with higher observation heights, which may be related to the lower resolution of visible and thermal infrared images and the greater classification error, especially at 120 m flight altitude.

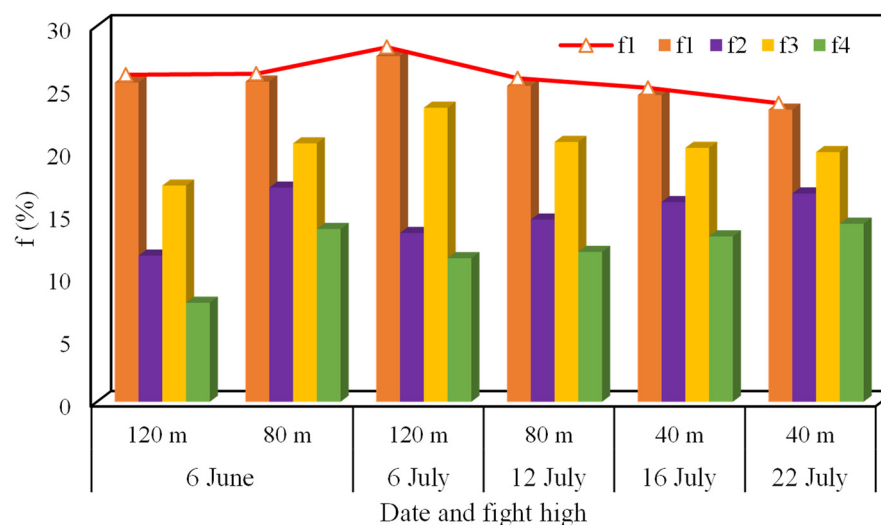


Figure 8. The temporal pattern histogram of vegetation coverage. The f1 and f2 represent the vegetation coverage of not considering and considering the shaded soil based on supervised classification, respectively; f3 and f4 represent the vegetation coverage of not considering and considering the shaded soil based on the supervised classification and normalized difference vegetation index (NDVI), respectively.

3.2.3. Vineyard Evapotranspiration Estimation

Based on the three-temperature model and UAV-based remote sensing technology, we quantified the evapotranspiration (Table 1). During the experiment period, the midday evapotranspiration values of the vineyard retrieved by remote sensing ranged from 93.14 to 271.30 $W \cdot m^{-2}$, and the ET1 to ET4 maintained a good correlation with the ground-measured values obtained by the EC system, with coefficients of determination between 0.64 and 0.74. Simultaneously, the results show that when the UAV-based images considered the shaded and mixed pixels in the classification, the RMSEs of ET estimated using multispectral or thermal infrared were 8.30 and 8.87, respectively, and the rRMSEs were 4.31% and 4.59%, respectively. When these pixels were not considered, the RMSEs of ET estimated using multispectral or thermal infrared were 22.46 and 24.98, respectively, and the rRMSEs were 10.52% and 11.41%, respectively. Thus, it can be concluded that ET estimated using multispectral together with consideration of shaded pixels has the highest accuracy. Among them, considering that the shaded pixels meant that the estimation accuracy of ET was improved by 4.59–6.82%, the estimation accuracy of ET after multispectral correction was improved by 0.28–0.89%. In a word, considering the shaded and mixed pixels had a greater impact on the estimation of the ET of the vineyard than modifying canopy cover using multispectral correction, the estimation accuracy improved significantly.

Table 1. The evapotranspiration ($W \cdot m^{-2}$) and accuracy of UAV remote sensing inversion under different scenarios.

Date	Fight High	EC System		f1		f2		f3		f4	
		ET	ET1	R ² /RMSE/ rRMSE	ET2	R ² /RMSE/ rRMSE	ET3	R ² /RMSE/ rRMSE	ET4	R ² /RMSE/ rRMSE	
6 June 2019	120 m	-	152.58		94.11		139.56		93.14		
	80 m	-	150.12		96.51		139.59		93.39		
6 July 2019	120 m	193.77	212.49	0.75/	201.19	0.63/	210.49	0.74/	200.64	0.64/	
12 July 2019	80 m	239.75	265.71	24.98/	241.41	8.87/	263.56	22.46/	245.48	8.30/	
16 July 2019	40 m	237.32	266.43	11.41%	252.13	4.59%	263.13	10.52%	250.97	4.31%	
26 July 2019	40 m	268.31	266.67		274.43		264.05		271.30		

Therefore, the spatial distribution of transpiration and evaporation using multispectral correction combined with eliminating shaded pixels is represented in Figure 9. Both evaporation and transpiration obviously had spatial heterogeneity, and this correlated with the land surface temperature, with the values mainly fluctuating between 200 and 300 $\text{W}\cdot\text{m}^{-2}$. Evaporation was slightly higher than transpiration, which was 238.05 and 208.79 $\text{W}\cdot\text{m}^{-2}$, respectively. Strong evapotranspiration capability of the vineyard implied the indispensability of optimal water resource allocation.

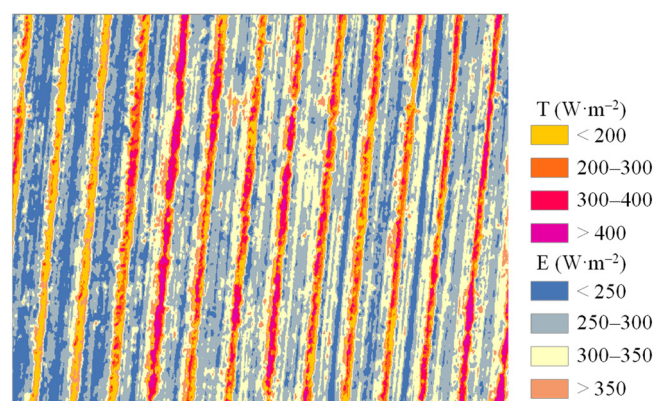


Figure 9. Spatial distribution of estimated values for the instantaneous transpiration and evaporation rate over a vineyard using UAV imagery and meteorological data on 16 July 2019.

3.3. Effect of the Shaded Vegetation Pixels on Vineyard Transpiration

3.3.1. Thermal Characteristics of Shaded Vegetation Pixels

We acquired the visible-light and thermal infrared images of the sunlit and shaded leaves of the grapevines at 10:30 h on 13 August 2020, as well as the canopy temperature frequency distribution (Figure 10). It can be gathered from the examples that the frequency distribution of leaf temperature showed a single-peak shape (Figure 10e) and, significantly, that the spatial distribution and frequency distribution of the sunlit and shaded leaves were different at the same time. The front peak represented the grape canopy temperature of shaded leaves, and the back peak represented the canopy temperature of sunlit leaves. To be more specific, the average canopy temperature of sunlit leaves was about 2 °C higher than that of shaded leaves. In the subsequent evaluation of grape water status using the 3T model, if the temperature difference of the three-dimensional structure of sunlit and shaded leaves was not considered, then the canopy temperature of grapes would be misestimated, resulting in less reliable assessments for water consumption.

3.3.2. Vineyard Plant Transpiration Estimation

To further assess the influence of sunlit and shaded grapevine leaves on water flux, based on the 3T model, the temperature from thermal infrared images was extracted at different moments in five days, and then the transpiration rates of sunlit and shaded leaves were quantified, respectively, as shown in Figure 11. The diurnal variation of transpiration showed a single-peak curve that first increased and then decreased. The peak transpiration rates of sunlit and shaded grapevine leaves were 0.44 and 0.37 mm/h, respectively. Meanwhile, there was a significant difference in T between sunlit and shaded leaves. During the observation period, the T of sunlit leaves was 6.45–91.67% larger than that of shaded leaves. The discrepancy between them was larger in the morning and afternoon and narrower at noon. After considering the three-dimensional structure of sunlit and shaded leaves in the vineyard, the calculated average transpiration was 0.26 mm/h, which was 7.44% lower than the average obtained from only considering sunlit leaves and 23.32% higher than the average when only considering shaded leaves.

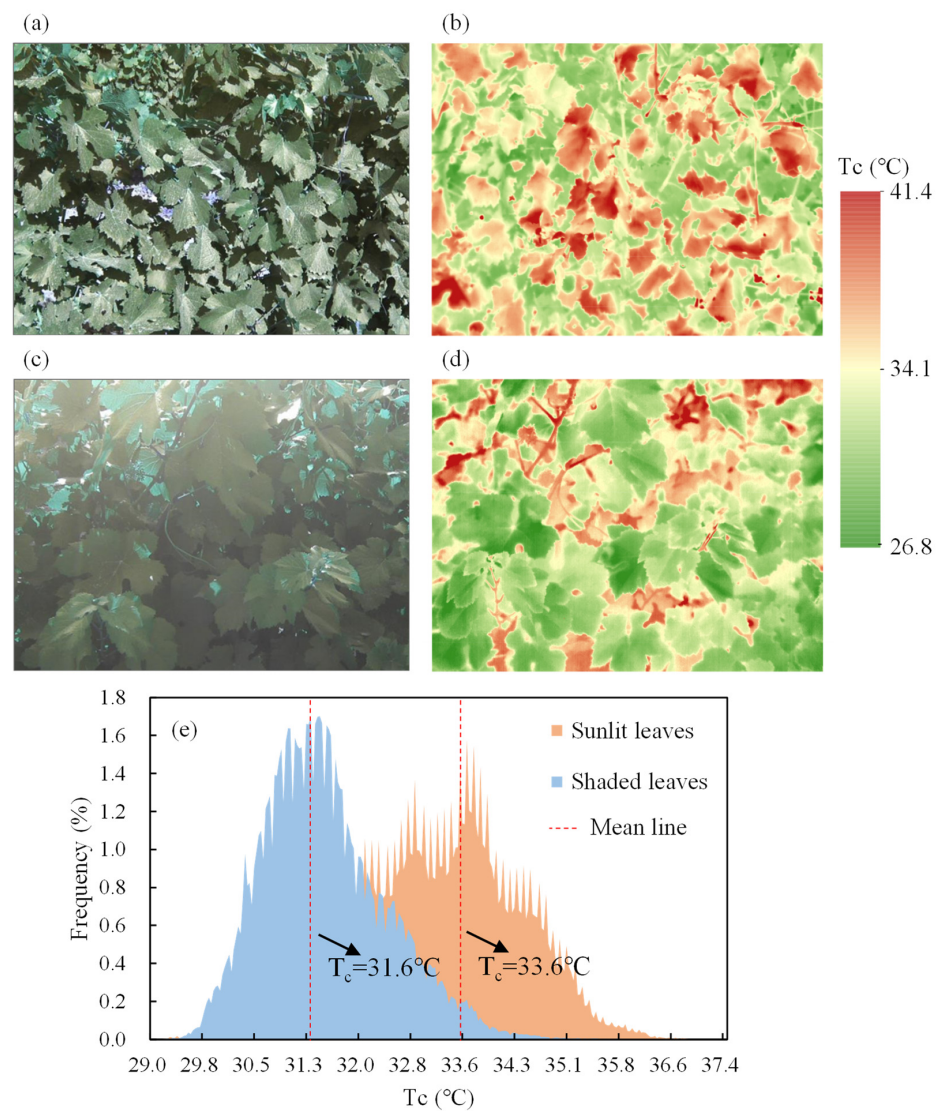


Figure 10. Illustration of the consequences of pixel binning for thermal image for the grape. (a,c) The RGB images; (b,d) the thermal images taken with a Fluke TiX620 camera; (e) together with corresponding frequency histograms of sunlit and shaded leaves. The images were taken at 10:30 on 13 August 2020.

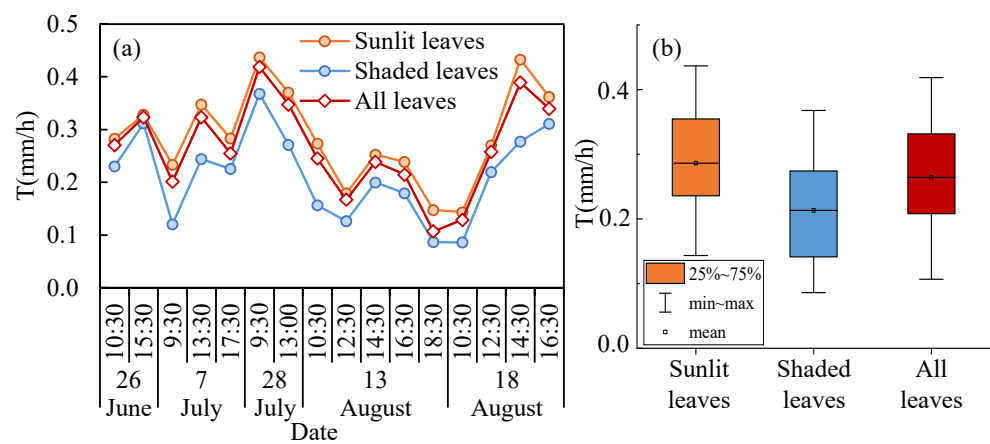


Figure 11. (a) Diurnal variations of transpiration rate of grape; and (b) the basic statistics of transpiration rate under sunlit leaves, shaded leaves, and all leaves.

A more detailed understanding of the advantage of considering the sunlit and shaded leaves is charted in Table 2. Verified with the T estimated by the EC system, the R^2 of ground-based remote sensing only considering sunlit leaves, only considering shaded leaves, and considering both sunlit and shaded leaves with EC were 0.83, 0.84, and 0.88, respectively; and the rRMSEs were 22.47%, 16.69%, and 15.31%, respectively, indicating that considering the sunlit and shaded leaves improved the estimation accuracy of T by 1.38–7.16%. Thus, the above results highlight the influence of the sunlit and shaded leaves on the quantification of grapevine transpiration, and, more importantly, demonstrate that the effectiveness of ground-based remote sensing measurements that reduce the influence of shaded leaves in a vineyard.

Table 2. Evaluation of transpiration rate (mm/h) accuracy of ground remote sensing inversion under different conditions.

Date	EC-T	Sunlit Leaves		Shaded Leaves		All Leaves	
		T	R^2 /RMSE/ rRMSE	T	R^2 /RMSE/ rRMSE	T	R^2 /RMSE/ rRMSE
26 June 2020	10:30	0.25	0.28	0.23		0.28	
	15:30	0.36	0.33	0.31		0.32	
7 July 2020	9:30	0.14	0.23	0.12		0.21	
	13:30	0.31	0.35	0.24		0.32	
	17:30	0.25	0.28	0.23		0.26	
28 July 2020	9:30	0.39	0.44	0.37		0.42	
	13:00	0.30	0.37	0.27		0.35	
13 August 2020	10:30	0.23	0.27	0.16		0.25	
	12:30	0.16	0.18	0.13		0.19	
	14:30	0.20	0.25	0.20		0.24	
	16:30	0.19	0.24	0.18		0.21	
	18:30	0.10	0.15	0.09		0.11	
28 August 2020	10:30	0.13	0.14	0.09		0.13	
	12:30	0.26	0.27	0.22		0.25	
	14:30	0.30	0.43	0.28		0.35	
	16:30	0.37	0.36	0.31		0.34	

4. Discussion

Tremendous work has been carried out by previous scientists to figure out one of the key challenges that all of viticulture is facing: water scarcity. Nowadays, precision agriculture is closely connected to the use of remote sensing technologies, which have been developed in response to the demand for digital technology [43], to manage the spatiotemporal patterns of farmland systems associated with agricultural water saving [44], including viticulture [1,29,30,40,42,45,46]. Researchers have made great and relevant advancements in monitoring water stress [40,46], vegetation indexes (e.g., NDVI [42], and leaf area index [45]). On the other hand, RS using UAVs has great potential for the inversion of water consumption. However, accurately extracting the pure crop and bare soil pixels remains a challenge due to the influences of shaded pixels [29,33]. The visible-light and thermal image characteristics of the shaded soil pixels at different observation heights were considered in this study. It can be gathered from the high-resolution RGB images that the shaded soil pixels were blurred and the number of mixed pixels grew with the increase of flight altitude (Figure 6). Corresponding to TIR images, with the increase of flight height, the frequency of shadow pixels increased from 0.07% (40 m) to 0.18% (120 m). Two shadow detection methods proved that increasing flight height resulted in increasing canopy cover if ignoring shadow (Figure 8), with values of f1 being 23.90%, 25.39%, and 26.54% at 40 m, 80 m, and 120 m observation height, respectively. Meanwhile, there were corresponding values of 16.28%, 15.82%, and 12.57%, respectively, if the shadow were removed. This validates the previous assumption that higher flight altitude would result in lower spatial resolution and more mixed and shaded pixels. Consequently, to produce suitable drone imagery, a flight height of 40 m or 80 m is recommended, and a low-altitude suggestion also results from these trials [47–49].

More recent studies have focused on the characteristics of pure pixels' water consumption [20,33]. Regarding the overlooked influence of shaded pixels on the estimation of ET, detailed analysis of the accuracy of such estimation has been performed in our study. Good linear fitting correlations and low errors were maintained with the EC system (Table 1). The R^2 of ET1, ET2, ET3, and ET4 with EC-ET were 0.75, 0.63, 0.74, and 0.64, respectively; the RMSEs of ET1, ET2, ET3, and ET4 with EC-ET were 24.98, 8.87, 22.46, and 8.30, respectively; and the rRMSEs of ET1, ET2, ET3, and ET4 with EC-ET were 11.41%, 4.59%, 10.52%, and 4.31%, respectively. These detailed findings provided strong evidence that the ET estimated using multispectral correction together with shaded pixels has the highest accuracy. This result could possibly be explained as follows. First of all, the essence of a shadow appears due to light being blocked [50], and the shaded area in aerial imagery may cause misunderstanding of valuable messages about actual features, such as shape, altitude, and color [27,33], which were captured in the RGB and thermal infrared images (Figure 6). Moreover, our results show that this darkening was caused by a decrease in the surface temperature of the soil pixels, so the effect of shadows increased the land cover classification error. Using our classification as an example, 7.8% and 30.6% of shadow and mixed pixels were divided into pure soil or pure vegetation pixels, respectively (Figure 7). Meanwhile, the mean-f1 and mean-f3 of ignored shadow pixels were 1.70 and 1.68 times that of the mean-f2 and mean-f4, respectively. As a result, the estimation of ET and its components were changed.

Surprisingly, the shadow detection process had a positive influence on the quantification of vineyard evapotranspiration, with the accuracy of ET being improved by 4.59–6.82%. Simultaneously, our results demonstrate that the spatial heterogeneity of ET can be seen in the vineyard (Figure 9), with the grapes being comparable to other crops such as peaches and nectarines that are grown in orchards [19] and upland rice [51]. Moreover, the mean evaporation and transpiration fluxes were 238.05 and 208.79 $W m^{-2}$, respectively, and crop transpiration accounted for 46.7% of evapotranspiration. The reason why this was different from the 57.2% of the global terrestrial ecosystem investigated by [7] may be explained by the fact that our research focus was a sparse vineyard.

Another type of shadow is the self-shadow, which is the part of the object not illuminated by direct light [50]. Tomas et al. [29] identified that the percentage of canopy-shaded pixels can reach as high as 43% for a vineyard, and our ground-based RGB image also implied this (Figure 10c). Furthermore, a 2 °C canopy temperature discrepancy was discovered between sunlit leaves and shaded leaves. Considering the three-dimensional structure in the estimation of grapevine transpiration, there was a significant difference in T between sunlit and shaded leaves, showing that the T of sunlit leaves was 6.45–91.67% higher than that of shaded leaves. In addition, the mean transpiration rate of total leaves was 0.26 mm/h, which was 7.44% lower than that of only sunlit leaves and 23.32% higher than that of only shaded leaves. Ultimately, the shadow detection process improved the estimation accuracy by 1.38–7.16%.

Our study highlights the detection and monitoring of vineyard water consumption with the consideration of shadow and successfully separated grape transpiration and soil evaporation using the 3T model. Supervised classification has been confirmed as an effective method to detect the shadow pixels by previous research [33], and our research innovatively took advantage of the NDVI obtained from multispectral imagery inversion to quantify the proportion of E and T in a vineyard ecosystem. Further research should systematically clarify other methods of shadow detection, such as the unsupervised classification method [20,52] and thresholding method [31,32].

5. Conclusions

This study innovatively combined UAV-based multispectral and thermal imagery and ground-based thermal imagery with the 3T model to provide a comprehensive assessment of shadow pixels on vineyard water consumption. More importantly, the shadow pixels in remotely sensed images were detected and considered. Two classes of shadow have

been discussed: the shaded soil and canopy. Our results confirm that the reliability of the assessment for ET and its components is significantly improved after considering shaded pixels, with high correlation and evaluation accuracy. The shadow detection process of shaded soil pixels improves the estimation accuracy of ET by 4.59–6.82%, and the shadow detection process of shaded canopy pixels improves the estimation accuracy of T by 1.38–7.16%. Moreover, we creatively combined NDVI-based canopy cover inversion with the 3T model to quantify the ET in a vineyard ecosystem, and our results indicate that the estimation accuracy was improved by 0.28–0.89%. Finally, the spatiotemporal variability of the vineyard was obtained. There was spatial heterogeneity of ET in the vineyard, and the mean E and T fluxes accounted for 238.05 and 208.79 W m⁻², respectively, indicating strong water consumption ability. The temporal pattern showed a single-peak curve that first increased and then decreased, with a mean of 0.26 mm/h. Our findings provide a better understanding of the influences of shadow pixels on ET estimation using remote sensing techniques, and other shadow detection methods should be further explored.

Author Contributions: Conceptualization, S.L., J.X. and F.T.; data curation, J.X., T.Z. and X.B.; formal analysis, S.L. and T.Z.; funding acquisition, J.X. and F.T.; investigation, J.X., T.Z. and X.B.; methodology, S.L., J.X., T.Z. and F.T.; project administration, F.T.; software, S.L.; supervision, F.T. and S.O.-F.; validation, X.B. and S.O.-F.; visualization, S.L.; writing—original draft, S.L.; writing—review and editing, F.T. All authors have read and agreed to the published version of the manuscript.

Funding: This work was supported by the National Natural Science Foundation of China (52179049), the international and regional cooperation and exchange projects of the National Natural Science Foundation of China (51961125205), and National Agency for Research and Development (ANID)/PCI (NSFC190013), the financial support provided by the Major Program of the National Natural Science Foundation of China (51790534).

Data Availability Statement: Not applicable.

Conflicts of Interest: All the authors declare no conflict of interest.

References

1. Su, B.; Xue, J.; Xie, C.; Fang, Y.; Fuentes, S. Digital surface model applied to unmanned aerial vehicle based photogrammetry to assess potential biotic or abiotic effects on grapevine canopies. *Int. J. Agric. Biol. Eng.* **2016**, *9*, 119.
2. Song, Z.W.; Sun, M.Y.; Yang, R.J.; Dou, G.Y.; Zhang, Y.; Zhang, L. Evaluation of ecosystem service value of the grape industry at the eastern foot of Helan Mountain, Ningxia, China. *J. Appl. Ecol.* **2019**, *30*, 979–985.
3. Zuniga-Espinoza, C.; Aspillaga, C.; Ferreyra, R.; Selles, G. Response of Table Grape to Irrigation Water in the Aconcagua Valley, Chile. *Agronomy* **2015**, *5*, 405–417. [[CrossRef](#)]
4. Yu, Z.; Hu, X.; Ran, H.; Wang, X.; Wang, W.; He, X. Estimation of grape evapotranspiration in semi-humid region based on Bowen ratio energy balance method. *Agric. Res. Arid Areas* **2020**, *38*, 175–183.
5. Zhang, K.; Kimball, J.S.; Running, S.W. A review of remote sensing based actual evapotranspiration estimation. *Wiley Interdiscip. Rev. Water* **2016**, *3*, 834–853. [[CrossRef](#)]
6. Rosenberg, N.J.; Black, B.L.V. *Microclimate: The Biological Environment of Plants*, 2nd ed.; John Wiley Sons: New York, NY, USA, 1983; p. 495.
7. Wei, Z.; Kei, Y.; Lixin, W.; Diego, G.M.; Scott, J.; Xuhui, L. Revisiting the contribution of transpiration to global terrestrial evapotranspiration. *Geophys. Res. Lett.* **2017**, *44*, 2792–2801. [[CrossRef](#)]
8. Jasechko, S.; Sharp, Z.D.; Gibson, J.J.; Birks, S.J.; Yi, Y.; Fawcett, P.J. Terrestrial water fluxes dominated by transpiration. *Nature* **2013**, *496*, 347–350. [[CrossRef](#)]
9. Lv, C.; Tan, J.; Chen, S.; Cui, Y. Real-time Forecast of Grape Evapotranspiration under Drip Irrigation in Hilly Region of Southern China. *J. Irrig. Drain.* **2012**, *31*, 47–52.
10. Vanino, S.; Pulighe, G.; Nino, P.; De Michele, C.; Bolognesi, S.F.; D’Urso, G. Estimation of Evapotranspiration and Crop Coefficients of Tendone Vineyards Using Multi-Sensor Remote Sensing Data in a Mediterranean Environment. *Remote Sens.* **2015**, *7*, 14708–14730. [[CrossRef](#)]
11. Yang, F.; Tian, J.; Zhu, H.; Shen, H. Effects of different drip irrigation methods and water and fertilizer combination on photosynthesis and yield of wine grape. *Water Sav. Irrig.* **2020**, *45*, 53–58.
12. Rana, G.; Katerji, N. Direct and indirect methods to simulate the actual evapotranspiration of an irrigated overhead table grape vineyard under Mediterranean conditions. *Hydrol. Process.* **2008**, *22*, 181–188. [[CrossRef](#)]
13. Wang, X. Study of the estimating methods for evapotranspiration in farmland. *Syst. Sci. Compr. Stud. Agric.* **2003**, *19*, 81–84.

14. Qiu, G.; Tomohisa, Y.; Kazuro, M. An improved methodology to measure evaporation from bare soil based on comparison of surface temperature with a dry soil surface. *J. Hydrol.* **1998**, *210*, 93–105. [[CrossRef](#)]
15. Brown, K.W.; Rosenberg, N.J. A Resistance Model to Predict Evapotranspiration and Its Application to a Sugar Beet Field. *Agron. J.* **1973**, *65*, 341–347. [[CrossRef](#)]
16. Yao, Y.; Chen, J.; Zhao, S.; Jia, K.; Xie, X.; Sun, L. Estimation of farmland evapotranspiration: A review of methods using thermal infrared remote sensing data. *Adv. Earth Sci.* **2012**, *27*, 1308–1318.
17. Hou, M.; Tian, F.; Zhang, T.; Huang, M. Evaluation of canopy temperature depression, transpiration, and canopy greenness in relation to yield of soybean at reproductive stage based on remote sensing imagery. *Agric. Water Manag.* **2019**, *222*, 182–192. [[CrossRef](#)]
18. Riveros-Burgos, C.; Ortega-Farias, S.; Morales-Salinas, L.; Fuentes-Penailillo, F.; Tian, F. Assessment of the clumped model to estimate olive orchard evapotranspiration using meteorological data and UAV-based thermal infrared imagery. *Irrig. Sci.* **2021**, *39*, 63–80. [[CrossRef](#)]
19. Park, S.; Ryu, D.; Fuentes, S.; Chung, H.; O’Connell, M.; Kim, J. Mapping Very-High-Resolution Evapotranspiration from Unmanned Aerial Vehicle (UAV) Imagery. *Isprs Int. J. Geo-Inf.* **2021**, *10*, 210. [[CrossRef](#)]
20. Ortega-Farias, S.; Esteban-Condori, W.; Riveros-Burgos, C.; Fuentes-Penailillo, F.; Bardeen, M. Evaluation of a two-source patch model to estimate vineyard energy balance using high-resolution thermal images acquired by an unmanned aerial vehicle (UAV). *Agric. For. Meteorol.* **2021**, *304*, 108433. [[CrossRef](#)]
21. Qiu, G.; Kazuro, M.; Tomohisa, Y. Estimation of Plant Transpiration by Imitation Leaf Temperature Theoretical consideration and field verification (I). *Trans. Jpn. Soc. Irrig. Drain. Reclam. Eng.* **1996**, *1996*, 401–410.
22. Qiu, G.; Wang, S.; Wu, X. Three temperature (3T) model—A method to estimate evapotranspiration and evaluate environmental quality. *Chin. J. Plant Ecol.* **2006**, *30*, 231–238.
23. Tian, F.; Qiu, G.; Yang, Y.; Lü, Y.; Xiong, Y. Estimation of evapotranspiration and its partition based on an extended three-temperature model and MODIS products. *J. Hydrol.* **2013**, *498*, 210–220. [[CrossRef](#)]
24. Xiong, Y.; Zhao, S.; Tian, F.; Qiu, G. An evapotranspiration product for arid regions based on the three-temperature model and thermal remote sensing. *J. Hydrol.* **2015**, *530*, 392–404. [[CrossRef](#)]
25. Hou, M.; Tian, F.; Zhang, L.; Li, S.; Du, T.; Huang, M.; Yuan, Y. Estimating Crop Transpiration of Soybean under Different Irrigation Treatments Using Thermal Infrared Remote Sensing Imagery. *Agronomy* **2018**, *9*, 8. [[CrossRef](#)]
26. Wei, J.; Yang, Y.; Xie, X.; Liao, L.; Tian, Y.; Zhou, J. Evapotranspiration estimation using three-temperature model and influencing factors of Nanning City, China. *J. Appl. Ecol.* **2021**, *32*, 289–298.
27. Ilkka, L.; Hamlyn, G.J. Combining thermal and visible imagery for estimating canopy temperature and identifying plant stress. *J. Exp. Bot.* **2004**, *55*, 1423–1431.
28. Zyl, J. Diurnal variation in grapevine water stress as a function of changing soil water status and meteorological conditions. *S. Afr. J. Enol. Vitic.* **2017**, *8*, 45–50.
29. Tomas, P.; Samuel, O.F.; Dongryeol, R. Automatic Coregistration Algorithm to Remove Canopy Shaded Pixels in UAV-Borne Thermal Images to Improve the Estimation of Crop Water Stress Index of a Drip-Irrigated Cabernet Sauvignon Vineyard. *Sensors* **2018**, *18*, 397.
30. Bellvert, J.; Zarco-Tejada, P.J.; Girona, J.; Fereres, E. Mapping crop water stress index in a ‘Pinot-noir’ vineyard: Comparing ground measurements with thermal remote sensing imagery from an unmanned aerial vehicle. *Precis. Agric.* **2014**, *15*, 361–376. [[CrossRef](#)]
31. Miura, H.; Midorikawa, S.; Fujimoto, K. Automated building detection from high-resolution satellite image for updating gis building inventory data. In Proceedings of the 13th World Conference on Earthquake Engineering, Vancouver, BC, Canada, 1–6 August 2004.
32. Heiskanen, J.; Kajuutti, K.; Jackson, M.; Elvehøy, H.; Pellikka, P. Assessment of glaciological parameters using landsat satellite data in svartisen, northern norway. In Proceedings of the EARSeL-LISSIG-Workshop Observing Our Cryosphere from Space, Bern, Switzerland, 11–13 March 2002.
33. Aboutaleb, M.; Torres-Rua, A.F.; Kustas, W.P.; Nieto, H.; Coopmans, C.; Mckee, M. Assessment of different methods for shadow detection in high-resolution optical imagery and evaluation of shadow impact on calculation of NDVI, and evapotranspiration. *Irrig. Sci.* **2019**, *37*, 407–429. [[CrossRef](#)]
34. Wu, Y.; Du, T. Estimating and partitioning evapotranspiration of maize farmland based on stable oxygen isotope. *Trans. Chin. Soc. Agric. Eng.* **2020**, *36*, 127–134.
35. Tian, F.; Qiu, G.; Lü, Y.; Yang, Y.; Xiong, Y. Use of high-resolution thermal infrared remote sensing and “three-temperature model” for transpiration monitoring in arid inland river catchment. *J. Hydrol.* **2014**, *515*, 307–315. [[CrossRef](#)]
36. Qiu, G.Y.; Yano, T.; Momii, K. Estimation of plant transpiration by imitation leaf temperature. II. Application of imitation leaf temperature for detection of crop water stress. *Trans. Jpn. Soc. Irrig. Drain. Rural Eng.* **1996**, *1996*, 245–246.
37. Qiu, G.; Momii, K.; Yano, T.; Robert, J.L. Experimental verification of a mechanistic model to partition evapotranspiration into soil water and plant evaporation. *Agric. For. Meteorol.* **1999**, *93*, 79–93. [[CrossRef](#)]
38. Zhao, S.; Yonghui, Y.; Guoyu, Q.; Qiming, Q.; Yunjun, Y.; Yujiu, X.; Chunqiang, L. Remote detection of bare soil moisture using a surface-temperature-based soil evaporation transfer coefficient. *Int. J. Appl. Earth Obs.* **2010**, *12*, 351–358. [[CrossRef](#)]
39. Qiu, G.; Ming, Z. Remotely monitoring evaporation rate and soil water status using thermal imaging and “three-temperatures model (3T Model)” under field-scale conditions. *J. Environ. Monit.* **2010**, *12*, 716–723. [[CrossRef](#)]

40. Baluja, J.; Diago, M.P.; Balda, P.; Zorer, R.; Meggio, F.; Morales, F.; Tardaguila, J. Assessment of vineyard water status variability by thermal and multispectral imagery using an unmanned aerial vehicle (UAV). *Irrig. Sci.* **2012**, *30*, 511–522. [[CrossRef](#)]
41. Zhou, Z.; Yang, Y.; Chen, B. Fractional vegetation cover of invasive *Spartina alterniflora* in coastal wetland using unmanned aerial vehicle (UAV) remote sensing. *Chin. J. Appl. Ecol.* **2016**, *27*, 3920–3926.
42. Kutnjak, H.; Leto, J.; Vranic, M.; Bošnjak, K.; Perčulija, G.; Pospišil, M. Potential of aerial robotics in crop production: High resolution NIR/VIS imagery obtained by automated unmanned aerial vehicle (UAV) in estimation of botanical composition of alfalfa-grass mixture. In Proceedings of the 50th Croatian and 10th International Symposium on Agriculture, Opatija, Croatia, 16–20 February 2015.
43. Xie, C.; Yang, C. A review on plant high-throughput phenotyping traits using UAV-based sensors. *Comput. Electron. Agric.* **2020**, *178*, 105731. [[CrossRef](#)]
44. Sassu, A.; Gambella, F.; Ghiani, L.; Mercenaro, L.; Pazzona, A.L. Advances in Unmanned Aerial System Remote Sensing for Precision Viticulture. *Sensors* **2021**, *21*, 956. [[CrossRef](#)]
45. Mathews, A.J.; Jensen, J.L. Visualizing and Quantifying Vineyard Canopy LAI Using an Unmanned Aerial Vehicle (UAV) Collected High Density Structure from Motion Point Cloud. *Remote Sens.* **2013**, *5*, 2164–2183. [[CrossRef](#)]
46. Santesteban, L.G.; Gennaro, S.; Herrero-Langreo, A.; Miranda, C.; Royo, J.B.; Matese, A. High-resolution UAV-based thermal imaging to estimate the instantaneous and seasonal variability of plant water status within a vineyard. *Agric. Water Manag.* **2017**, *183*, 49–59. [[CrossRef](#)]
47. Torres-Sanchez, J.; Pena, J.M.; de Castro, A.I.; Lopez-Granados, F. Multi-temporal mapping of the vegetation fraction in early-season wheat fields using images from UAV. *Comput. Electron. Agric.* **2014**, *103*, 104–113. [[CrossRef](#)]
48. Tu, Y.; Phinn, S.; Johansen, K.; Robson, A.; Wu, D. Optimising drone flight planning for measuring horticultural tree crop structure. *ISPRS J. Photogramm.* **2020**, *160*, 83–96. [[CrossRef](#)]
49. Minch, C.; Dvorak, J.; Jackson, J.; Sheffield, S.T. Creating a Field-Wide Forage Canopy Model Using UAVs and Photogrammetry Processing. *Remote Sens.* **2021**, *13*, 2487. [[CrossRef](#)]
50. Shahtahmassebi, A.R.; Yang, N.; Wang, K.; Moore, N.; Shen, Z. Review of shadow detection and de-shadowing methods in remote sensing. *Chin. Geogr. Sci.* **2013**, *23*, 403–420. [[CrossRef](#)]
51. Jin, H.; Fischer, B.; Rojasconejo, J.; Johnson, M.S.; Morillas, L.; Lyon, S.W.; Manzoni, S.; Garcia, M. Drone-Based Hyperspectral and Thermal Imagery for Quantifying Upland Rice Productivity and Water Use Efficiency after Biochar Application. *Remote Sens.* **2021**, *13*, 1866. [[CrossRef](#)]
52. Wang, S.; Hong, Z. Clustering-based shadow edge detection in a single color image. In Proceedings of the 2013 International Conference on Mechatronic Sciences, Electric Engineering and Computer (MEC), Shenyang, China, 20–22 December 2013; pp. 2057–2206.